

www.advenergymat.de

Modifying Li@Mn₆ Superstructure Units by Al Substitution to Enhance the Long-Cycle Performance of Co-Free Li-Rich Cathode

Zhibo Li, Yiwei Li, Mingjian Zhang,* Zu-Wei Yin, Liang Yin, Shenyang Xu, Changjian Zuo, Rui Qi, Haoyu Xue, Jiangtao Hu, Bo Cao, Mihai Chu, Wenguang Zhao, Yang Ren, Lin Xie,* Guoxi Ren,* and Feng Pan*

As one of the most promising cathodes for Li-ion batteries, Li-rich layered oxides suffer from low Coulombic efficiency, severe capacity fading, and voltage decay, which are related to the aggregated Li@Mn₆ superstructure units. Herein, a Co-free Li-rich oxide Li[Li_{1/4}Mn_{1/2}Ni_{1/6}Al_{1/12}]O₂ through Al substitution of Co in Li[Li_{1/4}Mn_{1/2}Ni_{1/6}Co_{1/12}]O₂, is designed. Combining the average structural refinement with the detailed local structural/chemical analysis, it is found that the introduced Al ions occupy the Mn sites in Li@Mn₆ superstructure units, which further induces the partial replacement of the central Li ions in Li@Mn₆ units by Ni²⁺. The modified superstructure units stabilize the anionic framework and suppress structural degradation during long-term cycling. A superior cyclability (a capacity retention of 91.4% after 500 cycles at 1 C) is achieved. This work not only deepens the understanding into the mechanism of Al substitution, but also provides a novel route to design high-performance Li-rich cathodes by modifying the local functional units.

Z. Li, Y. Li, M. Zhang, Z.-W. Yin, S. Xu, C. Zuo, R. Qi, H. Xue, J. Hu,

B. Cao, M. Chu, W. Zhao, F. Pan School of Advanced Materials

Peking University

Shenzhen Graduate School Shenzhen 518055, P. R. China

E-mail: zhangmj@pkusz.edu.cn; panfeng@pkusz.edu.cn

L. Yin, Y. Ren

X-ray Science Division Advanced Photon Source Argonne National Laboratory

Lemont, IL 60439, USA

Department of Physics

Southern University of Science and Technology

Shenzhen 518055, P. R. China E-mail: xiel3@sustech.edu.cn

G. Ren

State Key Laboratory of Functional Materials for Informatics Shanghai Institute of Microsystem and Information Technology Chinese Academy of Sciences

Shanghai 200050, China E-mail: gxren@mail.sim.ac.cn



The ORCID identification number(s) for the author(s) of this article can be found under https://doi.org/10.1002/aenm.202101962.

DOI: 10.1002/aenm.202101962

1. Introduction

Li-ion batteries (LIBs) have been regarded as one of the most efficient energy storage systems due to the high energy density and environmentally friendliness. The demand for LIBs with higher energy density becomes imperative facing to the rapid expansion of electronic device and electric vehicle markets.[1-3] The energy density of LIBs system is largely determined by the performance of the cathode materials.^[4] Li-rich layered oxides, xLi₂MnO₃·yLiMO₂ (M = Mn, Ni, Co, Fe, etc.), have been considered as the next-generation cathode materials owing to the high specific capacity (>250 mA h g⁻¹) and energy density (>900 W h kg⁻¹).^[5,6] Nevertheless, a few shortages greatly restrict their industrialization.[7] First, the severe Li/O

loss in the initial cycle results in a low initial Coulombic efficiency.^[8] Most importantly, with the constant Li/O loss at high potentials, transition metal (TM) ions in TM layers will irreversibly migrate into Li layers, causing the formation of spinel phase. The spinel structure formed at the surface will gradually spread into the bulk during long-term cycling, resulting into a severe capacity and voltage degradation.^[9,10] To solve such problems, a few methods have been attempted, including element doping, morphology regulation, surface coating, etc.^[11–13] Compared with other methods, element doping has less process complexity and can be easily implanted into the traditional high-temperature synthesis.

Actually, the shortages for Li-rich cathodes mentioned above can be attributed to the over-activated oxygen ions, which are originated from the unique 180° Li-O-Li configuration due to the aggregated Li@Mn₆ superstructure units in TM layers.^[14-16] Therefore, the modification of Li@Mn₆ superstructure units has become an effective method to promote the electrochemical performance of Li-rich cathodes. Cho et al. reported that more reversible oxygen redox could be achieved in Li_{1.15}Mn_{0.51}Co_{0.17}Ni_{0.17}O₂ by dispersing the extra Li ions of Li@Mn₆ superstructure units in TM layers.^[17] Xie et al. discovered that Li ions in Li₂MnO₃ (LMO) component of Li_{1.2}Mn_{0.56}Ni_{0.16}Co_{0.08}O₂ could be partly replaced by

www.advancedsciencenews.com

www.advenergymat.de

16146849, 2021, 37, Downloaded from https://advanced onlinelibrary.wiely.com/doi/10.1002/aema.020101962 by University Town Of Shenzhen, Wiley Online Library on [2411.0225]. See the Terms and Conditions (https://onlinelibrary.wiely.com/terms-and-conditions) on Wiley Online Library for rules of use; OA archies are governed by the applicable Centwise Commons I

Na ions, which manipulated the local electronic structure of Li@Mn6 superstructure units and made Na/F co-doped $\mathrm{Li}_{(1.2-\gamma)}\mathrm{Na}_{\gamma}\mathrm{Mn}_{0.56}\mathrm{Ni}_{0.16}\mathrm{Co}_{0.08}\mathrm{O}_{(2-z/2)}\mathrm{F}_{z} \ \, \mathrm{display} \ \, \mathrm{a} \ \, \mathrm{higher} \ \, \mathrm{reverssor}$ ible capacity and a better capacity retention.[18] It is noticed that, Al doping has been extensively adopted to promote the electrochemical performance of Li-rich layered cathodes in the past decade. [19-24] Dianat et al. found that Al doping could stabilize layered structure and inhibit irreversible structural variation in Li-rich cathodes through theoretical calculations.^[25] Li et al. reported the first Al substituted Li-rich cathode $Li_{1.2}Ni_{0.16}Mn_{0.56}Co_{0.08-\nu}Al_{\nu}O_2$ in 2012, showing the promoted cyclability and thermal stability.[26] Nayak et al. doped Li_{1,2}Ni_{0,16}Mn_{0,56}Co_{0,08}O₂ by Al on the account of Mn. Although the initial capacity decreased after Al substitution, the capacity and voltage decay had been greatly reduced, which could be attributed to the suppressed layered-spinel phase transition during cycling.^[19] Although these successful cases of Al doping in promoting the electrochemistry, the detailed impacts of Al doping on the local structure, especially the modification on the Li@Mn₆ superstructure units, have not been understood experimentally.

Herein, we synthesize a novel Co-free Li-rich layered cathode Li[Li_{1/4}Mn_{1/2}Ni_{1/6}Al_{1/12}]O₂ (LMNA) through the complete Al substitution of Co in Li[Li_{1/4}Mn_{1/2}Ni_{1/6}Co_{1/12}]O₂ (LMNC). Combining the synchrotron X-ray diffraction (SXRD), scanning transmission electron microscopy (STEM), and X-ray absorption spectroscopy (XAS), the specific site of Al ions and the local structure changes after Al substitution are clarified. The introduced Al ions occupy the 4g (Mn) sites of Li@Mn₆ superstructure units and further cause the partial replacement of Li ions of Li@Mn₆ superstructure units by Ni²⁺. The modified Li@Mn₆ superstructure units disperse the extra Li ions in TM layers and break up the aggregated Li-O-Li configuration. Consequently, LMNA exhibits more reversible oxygen redox and less phase transition during the long-term cycling compared with LMNC. A superb long-term stability, 91.4% of capacity retention after 500 cycles at 1 C is achieved. This work provides a new way to stabilize the layered structure of Li-rich cathodes by tuning Li@Mn₆ superstructure units with element doping.

2. Results and Discussion

2.1. Modifying Li@Mn6 Superstructure Units by Al Substitution

As shown in Table S1 in the Supporting Information, the element ratios in LMNC and LMNA by inductively coupled plasma optical emission spectrometer (ICP-OES) measurement are well consistent with the theoretical values. The scanning electron microscope (SEM) images of the as-prepared LMNC and LMNA (Figure S1, Supporting Information) demonstrated no obvious morphology variation after Al substitution. Both exhibit the aggregated primary particles with the size around 200 nm. SEM-EDS (energy dispersive spectrometer) and TEM-EDS results (Figures S2 and S3, Supporting Information) confirm the uniform distribution of Al ions in LMNA. Similar X-ray diffraction (XRD) patterns of LMNC and LMNA (Figure S4a, Supporting Information) demonstrated that, both of LMNC and LMNA exhibited the well crystallized

layered structure. Rietveld refinements were performed using the trigonal layered structure model with space group $R ext{-}3m$. The refined parameters are summarized in Table S2 in the Supporting Information. Parameters a and c become slightly larger after Al substitution, which is well consistent with the previous reports. High-resolution TEM (HRTEM) images and the corresponding fast Fourier transform (FFT) maps of LMNC and LMNA are shown in Figure S4b,c in the Supporting Information. Stacked atomic layers could be clearly observed along the c direction for both LMNC and LMNA, further demonstrating their high crystallinity.

To further explore the influence of Al substitution on the fine crystal structure, SXRD pattern of LMNA was collected, and Rietveld refinement was performed using the monoclinic layered structure model with space group C2/m (Figure 1a and Table S3, Supporting Information). First, we tried to refine Al co-occupancy with Li at 2c and 4h sites in Li layers, and found no Al occupancy at 4h site and little Al occupancy (≈0.02) at 2c site. Negligible TM or Al occupancy in Li layers was further confirmed by the HRTEM image in Figure 1d. Based on these results, no TM and Al occupancy in Li layers was assumed to simplify the structural model for the further refinement. Then we can focus on refining the distribution of Li/Mn/Ni/Al at 2b and 4g sites in TM layers in the fixed atomic ratio according to the formula Li[Li_{1/4}Mn_{1/2}Ni_{1/6}Al_{1/12}]O₂. Assuming the 2b and 4g sites are both fully occupied, the occupancies of Li/Mn/Ni/Al at 2b site are complementary to those at 4g site. A series of refinements were performed with the varied Li occupancy at 2b site, and the meaningful occupancy values at 2b and 4g sites (1> all occupancies >0) were obtained and plotted in Figure 1b,c. It is clear that, Ni occupancies at 2b and 4g sites are around 0.4 and 0.05, respectively, showing low relevance with the Li occupancy at 2b site. It can be deduced that, almost 80% of Ni took the 2b site, namely, the central Li site in Li@Mn₆ superstructure units after Al substitution, which are consistent with the lower valence state of Ni close to +2 as demonstrated by XAS below, leading to serious Li⁺/Ni²⁺ mixing. Surprisingly, the Al occupancy at 2b site exhibits the negative relationship with the Li occupancy at 2b site. Considering the big radius difference between Li⁺ (0.76 Å) and Al3+ (0.535 Å), it is more reasonable, Al3+ mainly takes 4g site, namely, Mn site in Li@Mn₆ superstructure units, which agrees well with the previous theoretical calculations. [20,25] In brief, 2b (Li) sites in Li@Mn₆ superstructure units were mainly took up by 53% Li and 41% Ni, while 4g (Mn) sites in Li@Mn₆ superstructure units are mainly occupied by 73% Mn, 12% Al, and 11% Li, based on the refinement results.

To prove the modification in Li@Mn₆ superstructure units, the local structure at atomic scale of LMNA was further examined by STEM high-angle annular dark-field (HAADF) imaging. As shown in Figure 1d. The bright layers can be assigned to TM layers owing to the high scattering ability of TM cations, and the dark layers in between should be Li layers. No bright atoms could be observed in Li layers, hinting few Li/TM antisite between Li and TM layers, which is consistent with the refinement results above. For most of the TM layers, two bright dots and one dark dot alternately arrange, implying the Mn/Mn/Li ordering arrangement in Li@Mn₆ superstructure units (inset of Figure 1e). However, part of the TM layers filled with bright dots could also be observed, which are marked by blue

16146840, 2021, 37, Downloaded from https://advancec

.com/doi/10.1002/aenm.202101962 by University Town Of Shenzhen, Wiley Online Library on [24/11/2025]. See the Terms

and-conditions) on Wiley Online Library for rules of use; OA articles are governed by the applicable Creative Commons

www.advancedsciencenews.com

www.advenergymat.de

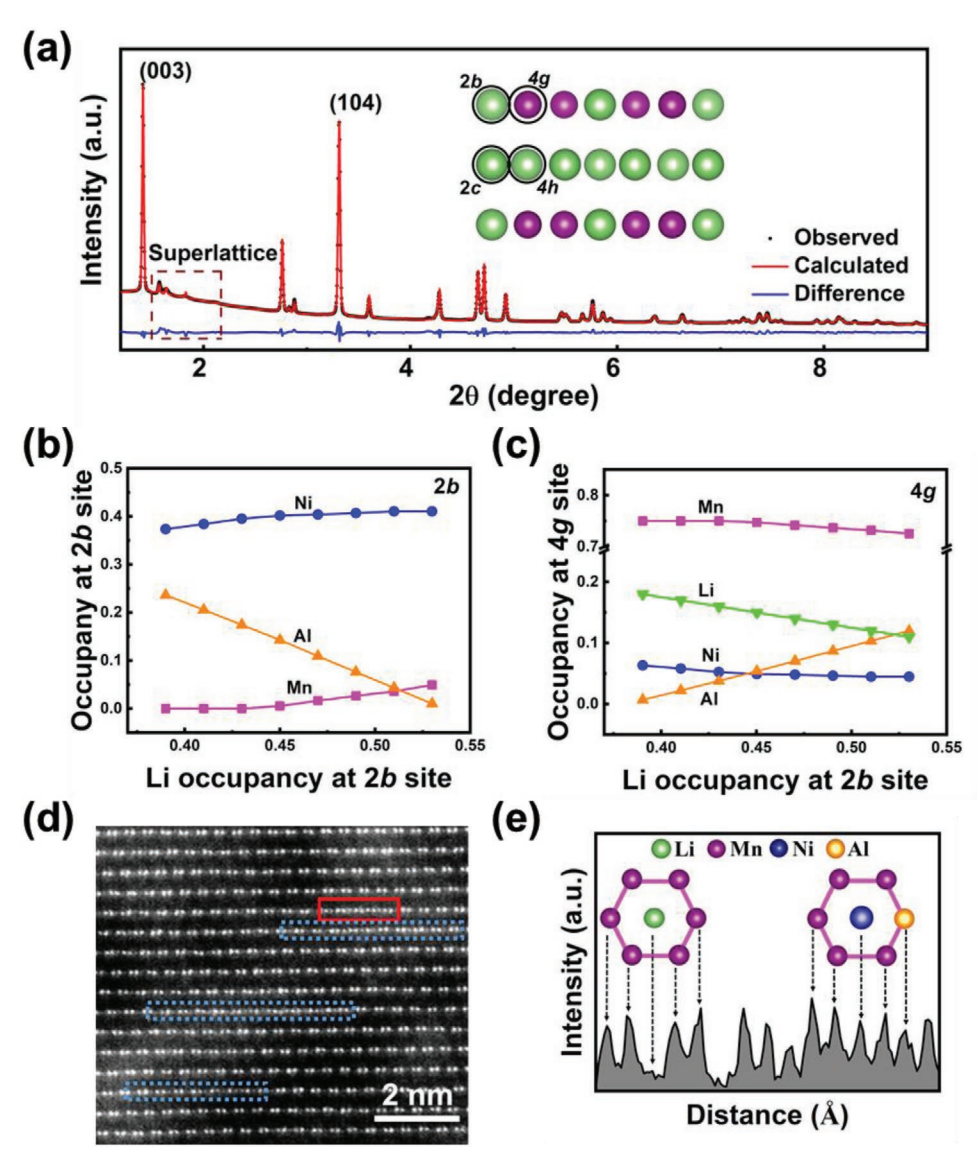


Figure 1. The local structural modification by Al substitution. a) SXRD pattern and the corresponding Rietveld refinement results of LMNA oxide. b) The refined occupancies of Ni, Mn, and Al at 2b site as a function of the Li occupancy at 2b site. c) The refined occupancies of Ni, Mn, Al, and Li at 4g site as a function of the Li occupancy at 2b site. d) STEM-HAADF image of LMNA along the *c*-direction. e) The scattering intensity of the ions in the region marked by red rectangle in (d).

rectangles. The intensity profile in the region marked by the red rectangle of Figure 1d is shown in Figure 1e. Combining the scattering intensities of Ni/Mn/Al/Li and the SXRD refinement results about Al sites, the atomic type corresponding to each intensity peak can be deduced. Five continuous strong peaks on the right could be assigned to the modified Li@Mn₆ superstructure units, in which part of the Mn ions are substituted by Al ions and the central Li ions are partly replaced by Ni cations.

The local structure change can be summarized here. Al ions occupied the 4g (Mn) sites in Li@Mn $_6$ superstructure units and further caused Li/Ni antisite in TM layers. Thus, the Li@Mn $_6$ superstructure unit evolved to (Li/Ni)@(Mn/Al/Li) $_6$. Such modification in Li@Mn $_6$ superstructure units may greatly impact the electrochemical performance, since the oxygen redox activity is closely correlated with Li@Mn $_6$ superstructure units. [28]

2.2. The Local Structural Change

To further examine the local structural changes, the XAS measurements for the transition metal cations and Al ions in LMNC and LMNA have been performed. The Mn L-edge soft XAS (sXAS) spectra for LMNC and LMNA and the reference spectra of Mn⁴⁺ (Li₂MnO₃) were taken in the total electron yield (TEY) mode in Figure S5 in the Supporting Information. The similar profiles and the same peak positions marked by the two dashed vertical lines demonstrated that the Mn valence states in LMNC and LMNA are both +4. It was further confirmed by the X-ray absorption fine structure (XAFS) spectra of Mn K-edge for LMNC and LMNA (Figure S6a, Supporting Information), indicating no influence of Al substitution on the chemical state of Mn. The Ni L-edge sXAS spectra in both TEY and total

16146840, 2021, 37, Downloaded from https://advanced.onlinelibrary.wiley.com/doi/10.1002/aenm.202101962 by University Town Of Shenzhen, Wiley Online Library on [24/11/2025]. See the Terms

and Conditions (https://onlinelibrary.wiley.com/terms-and-conditions) on Wiley Online Library for rules of use; OA articles are governed by the applicable Creative Commons I

www.advancedsciencenews.com

www.advenergymat.de

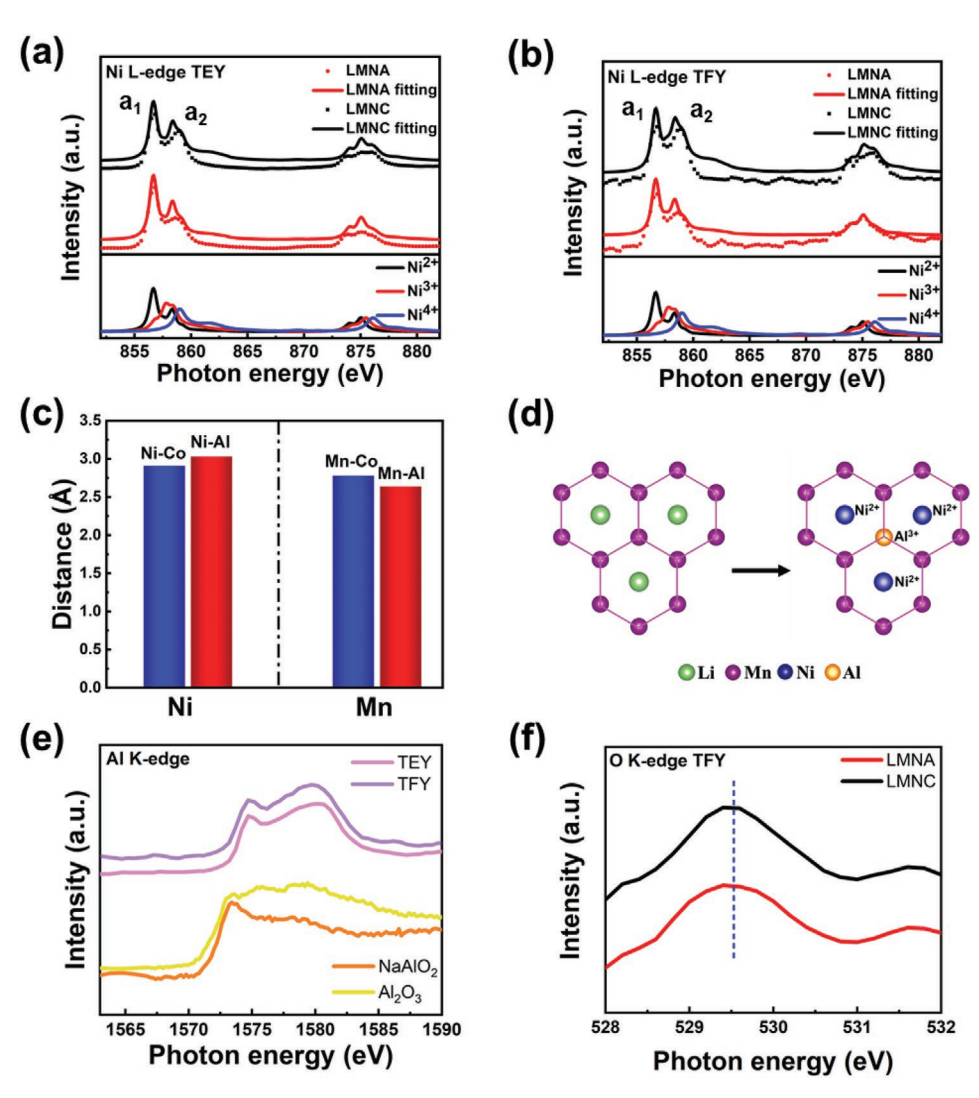


Figure 2. The local chemical and structural impacts by Al substitution. The sXAS spectra of Ni L-edge for LMNC and LMNA in a) TEY mode and b) TFY mode. Reference spectra of Ni^{2+} , Ni^{3+} , and Ni^{4+} were taken to identify the valence states. c) The Ni–Co and Mn–Co distances in LMNC, and the Ni–Al and Mn–Al distances for LMNA obtained from the fitting results of the corresponding EXAFS spectra (Tables S4 and S5, Supporting Information). d) Atomic arrangement in the TM layer of LMNA. e) XAS spectra of Al K-edge for LMNC and LMNA. Reference spectra of NaAlO₂ and Al₂O₃ are used as the references. f) X-ray absorption near edge spectroscopy spectra of O K-edge in TFY mode for LMNC and LMNA enlarged from Figure S8b in the Supporting Information.

fluorescence yield (TFY) modes were collected to analyze the impacts on Ni chemical states (Figure 2a,b). The spectra are dominated by the 2p core-hole spin-orbit coupling which splits the spectra roughly into two parts, namely, L3 and L2. And the L_{3,2} edge presents a typical multiplet structure, which is due to the various Coulomb and exchange interactions and crystalfield splitting. [29,30] The peak intensity ratio of a_1 and a_2 peak (a_1/a_2) can be used to indicate the charge valence of Ni.^[31,32] The increased a_1/a_2 value for LMNA as compared to LMNC can be observed, meaning a decreased valence state of Ni both at the surface and in the bulk after Al substitution. Besides, the similar phenomenon could also be found in the Ni K-edge XAFS spectra for LMNC and LMNA in Figure S7a in the Supporting Information. Through the linear combination fitting using the reference spectra calculated through the multiplet theory, [31] the mean oxidation states of Ni at the surface and in the bulk of LMNA were deduced as +2.5 and +2.6, respectively. More Ni^{2+} after Al substitution was responsible for the serious cationic mixing between Ni^{2+} and Li^+ revealed by the refinement above, due to the similar ionic radii of Ni^{2+} (0.69 Å) and Li^+ (0.76 Å). It is also rational that, Al^{3+} substitution at 4g (Mn⁴⁺) sites in $\mathrm{Li}@\mathrm{Mn}_6$ superstructure units would decrease the local electron density, which induced Ni^{2+} to take the central Li^+ site for the local charge neutralization. In addition, the co-existence of Ni^{4+} and Ni^{2+} aims to maintain the overall charge balance after the complete Al^{3+} substitution of Co^{3+} .

To further clarify the Li/Ni antisite in TM layers of LMNA, Ni and Mn extended X-ray absorption fine structure (EXAFS) analysis was performed in Figures S6 and S7 in the Supporting Information. The detailed fitting parameters are listed in Tabled S4 and S5 in the Supporting Information. The Ni–Co and Mn–Co distances in LMNC and the Ni–Al and

16146840, 2021, 37, Downloaded from https://advanced

.com/doi/10.1002/aenm.202101962 by University Town Of Shenzhen, Wiley Online Library on [24/11/2025]. See the Terms

and Conditions (https://onlinelibrary.wiley.com/terms

and-conditions) on Wiley Online Library for rules of use; OA articles are governed by the applicable Creative Commons

www.advancedsciencenews.com

www.advenergymat.de

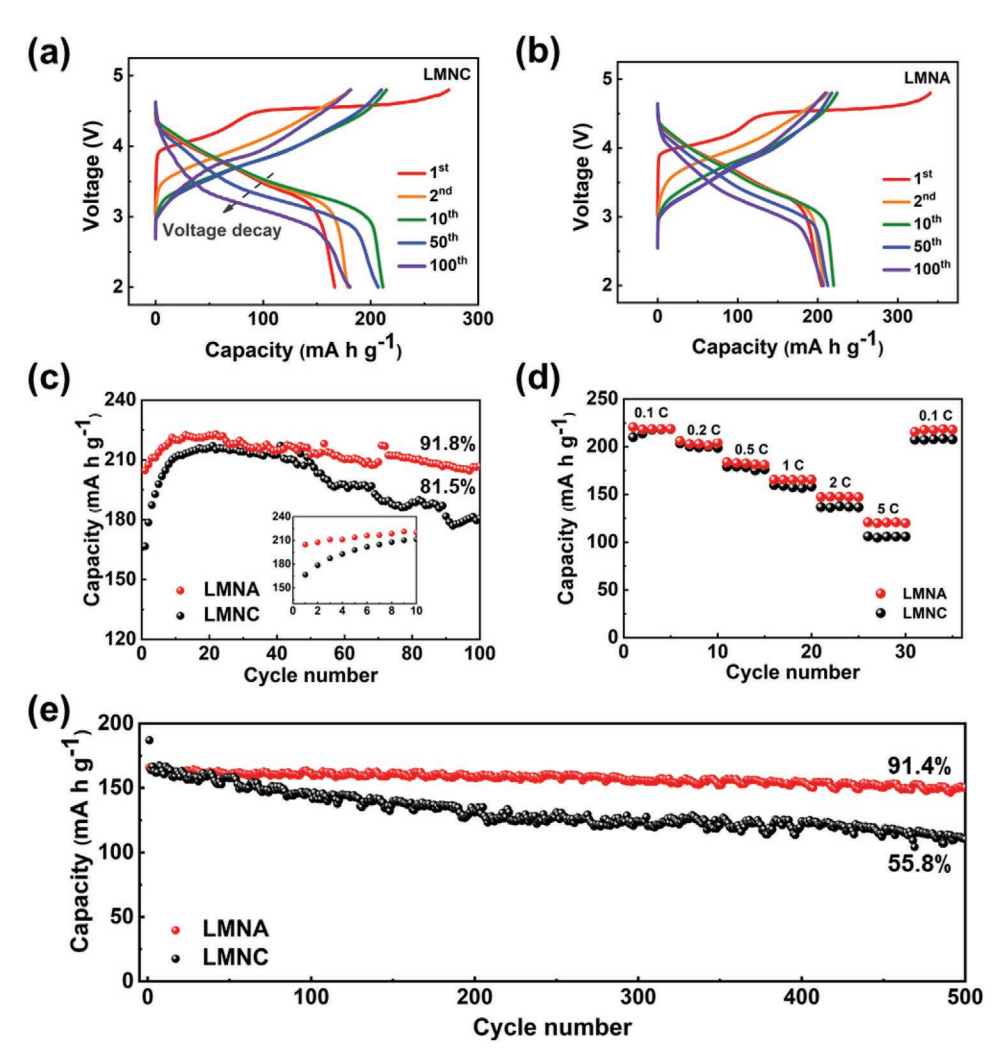


Figure 3. The promoted electrochemical performance by Al substitution. The capacity–voltage profiles at 1st, 2nd, 10th, 50th, 100th cycles of a) LMNA and b) LMNC. c) Cycling performance for LMNC and LMNA at 0.1 C (20 mA g^{-1}). The inset shows the activation process in the first several cycles. d) The rate performance of the LMNC and LMNA cathodes. e) Cycling performance of LMNC and LMNA cathodes at 1 C.

Mn–Al distances in LMNA were compared in Figure 2c. After Al substitution, Ni–Al distance increased than Ni–Co distance, while Mn–Al distance decreased than Mn–Co distance. It can be concluded that Ni and Mn are not located at the same site in LMNA, which supports the hypothesis about Ni occupying the central Li⁺ site in Li@Mn₆ superstructure unit. Hence, combining the SXRD, STEM-HAADF, sXAS, and EXAFS results together, the local structural changes can be further clarified. As shown in Figure 2d, in the modified Li@Mn₆ superstructure units, Ni²⁺ would take the central Li⁺ site to balance the local charge, making the Li ions in TM layers distribute more uniformly.

To investigate the coordination environment of Al ions, the Al K-edge sXAS spectra in TEY and TFY modes for LMNA are compared with those for NaAlO₂ and Al₂O₃. Al is coordinated by four oxygen atoms and six oxygen atoms in NaAlO₂ and Al₂O₃, respectively. Similar profiles for LMNA and Al₂O₃ hint Al at octahedral sites in LMNA. Moreover, the absorption edge for LMNA shifts to the high energy direction compared with that for NaAlO₂ and Al₂O₃, hinting the stronger Al–O bond in LMNA. The O K-edge sXAS spectra in TEY and TFY modes for

LMNC and LMNA are shown in Figure S8 in the Supporting Information, and the region marked by gray dashed rectangle is enlarged in Figure 2f. The spectrum for LMNA is low-energy shifted comparing with that of LMNC, which reflects the impact of Al substitution on the oxygen anionic lattice. It was usually considered as the cause for the better structure stability after Al substitution.^[23]

2.3. The Superior Cycling Stability

The electrochemical performance of LMNC and LMNA cathode are systemically compared in **Figure 3**. The capacity–voltage profiles of LMNC and LMNA cathodes at 1st, 2nd, 10th, 50th, 100th cycle are shown in Figure 3a,b, respectively. Similar initial charge profiles were presented for LMNC and LMNA. The slope below 4.45 V and the long plateau above 4.45 V result from the TM redox and oxygen activation, respectively. [34] The contribution of the long plateau above 4.45 V to the whole charging capacity for LMNA (63.62%) is less than that of LMNC (68.12%,

www.advancedsciencenews.com

www.advenergymat.de

16146840, 2021, 37, Downloaded from https://advanced.onlinelibrary.wiky.com/doi/10.1002/senm.202101962 by University Town Of Shenzhen, Wiley Online Library on [2411/2025]. See the Terms and Conditions (https://onlinelibrary.wiky.com/

and-conditions) on Wiley Online Library for rules of use; OA articles are governed by the applicable Creative Commons

Table S6, Supporting Information), implying the over-high oxygen redox activity might be suppressed by Al substitution. A similar phenomenon could be observed in cyclic voltammetry (CV) results (Figure S9, Supporting Information). After Al substitution, the intensity ratio between oxygen activation peak and TM redox peak decreased, further demonstrating the suppressed oxygen activity in LMNA during the initial cycling. In addition, a little peak could be found about 4.6 V at the second cycle in LMNC, which cannot be observed in LMNA, demonstrating the enhanced reversibility of oxygen redox after the Li@Mn6 superstructure units were modified. Therefore, the severe capacity and voltage decay (marked by the dashed arrow) in LMNC have been partly suppressed in LMNA. The cycling performance of LMNC and LMNA at 0.1 C (20 mA g⁻¹) is compared in Figure 3c. After an activation process in the first ten cycles (inset in Figure 3c), LMNC and LMNA exhibit the similar specific capacity, about 220 mA h g⁻¹. Although the inactive Al ions replace the active Co ions, the lower valence of Ni in LMNA could provide extra capacity to compensate the capacity loss. After 100 cycles, a high capacity retention of 91.8% can be achieved for LMNA, much higher than that for LMNC (81.5%). In addition, the average voltage decay for LMNA after 100 cycles is 0.38 V, less than that of LMNC (0.46 V, Figure S10, Supporting Information), demonstrating that, the voltage decay is partly suppressed by Al substitution. The rate performance (tested after ten cycles activation) is also promoted after Al substitution (Figure 3d), especially at the high rate 5 C, which may be partially ascribed to the smaller impedance of LMNA than that of LMNC (Figure S11, Supporting Information). The cycling stability at high rate 1 C was further tested (Figure 3e). The capacity retention is 91.4% after 500 cycles, meaning less than 0.02% of capacity loss in each cycle.

2.4. The Suppressed Structure Variation during the Initial Cycle

The promoted electrochemical performance should be originated from the more stable crystal structure during cycling. To investigate the structural changes during the initial charging—discharging process, the in situ SXRD experiments for LMNC and LMNA cathodes were performed (**Figure 4**). The variation of (003), (104), and (113) peaks during the initial cycling are shown in Figure 4a–d. (003) peaks for LMNC and LMNA constantly shift to the low angle below 4.45 V, corresponding to the lattice expansion

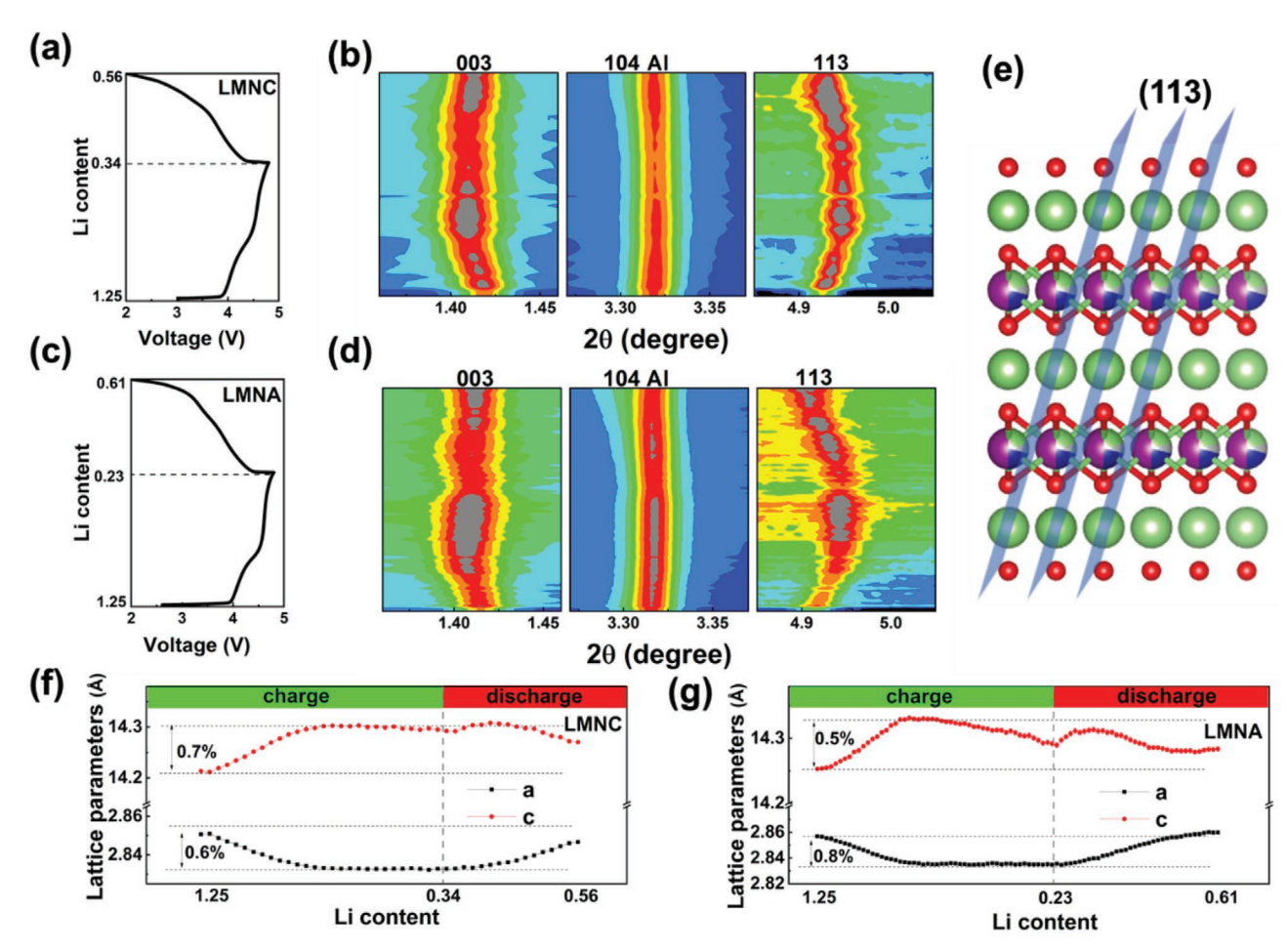


Figure 4. The structural variations during the first cycle. The a) charge/discharge curve as well as b) the in situ SXRD patterns of LMNC during the first cycle. The c) charge/discharge curve as well as d) the in situ SXRD patterns of LMNA during the first cycle. e) The illustration of (113) plane in the layered structure. Evolution of the lattice parameters as a function of charge/discharge state for f) LMNC and g) LMNA. The values were obtained from Rietveld refinement of in situ SXRD data.

ADVANCED ENERGY MATERIALS

www.advancedsciencenews.com

www.advenergymat.de

16146840, 2021, 37, Downloaded from https://advanced.onlinelibrary.wiley.com/doi/10.1002/aemm.202101962 by University Town Of Shenzhen, Wiley Online Library on [2411/2025]. See the Terms and Conditions (https://onlinelibrary.wiley.com/terms-and-conditions) on Wiley Online Library for rules of use; OA aricles are governed by the applicable Cerative Commons

along the c axis due to the increased electrostatic repulsion with Li⁺ deintercalation. When charged above 4.45 V, (003) peaks keep nearly unshifted, and even shift slightly to the high angle for LMNA, due to the reduced electrostatic repulsion involving O redox. [35,36] The (104) peaks are overlapped with Al (200) peak, and present the shift trend to the low angle when discharged to 2.0 V. Furthermore, (113) peaks are monitored to explore the variation in ab plane for LMNC and LMNA during the initial cycling since the corresponding (113) crystallographic plane runs through the ab plane (Figure 4e). It exhibits the reverse shift trend as (003) peak for both LMNC and LMNA, moving to higher angle during charge and to lower angle during discharge. It hints the opposite change trend along ab plane as compared with that along the c axis.

Quantitative analysis was performed through the Rietveld refinement with space group R-3m. The refined lattice parameters a and c for LMNC and LMNA are presented in Figure 4f,g, respectively. Although both of a and c for LMNC and LMNA exhibit similar change trend, the change extent of parameter c for LMNA (0.5%) is smaller than that of LMNC (0.7%), while the change extent of parameter a for LMNA (0.8%) is larger than that of LMNC (0.6%). It may hint that the structural stability is largely decided by the variation of parameter c rather than that of parameter a. In addition, a and c for LMNA after the first cycle can approach the initial values before cycling as compared with those of LMNC, indicating the enhanced structural reversibility by Al substitution. Figure S12 in the Supporting Information exhibits the volume changes during the first cycle for LMNC and LMNA. Interestingly, the volume variation for LMNA is a little larger than LMNC, indicating that the stability of phase structure may not be related to the volume change, but mainly depends on the change of c direction. The larger volume change of LMNA comes from the larger change of parameter a (Figure 4f,g). It can be ascribed to the intensive variation of TM layers along ab plane with the extraction/insertion of Li ions since Al ions with the stronger Al-O bonding are introduced into the TM layers of LMNA. In summary, the modified Li@Mn6 superstructure units after Al substitution decrease the variation degree along the c direction and stabilize the layered structure during the initial cycling.

2.5. The Suppressed Structural Degradation after Long-Term Cycling

To further explore the reason for the promoted electrochemical performance by the modified Li@Mn₆ superstructure units, the long-term cycling behavior of the LMNC and LMNA cathodes has been researched. CV results at the 1st, 2nd, 10th, 50th, and 100th cycle of LMNC and LMNA cathodes are shown in Figure S13 in the Supporting Information. For the oxidation branch, two new peaks have gradually appeared with the increased cycles, one at 3.1 V and the other at 4.4 V (marked by the dashed arrows). The former is related to the formation of Mn-based spinel phase. [37] For the reduction branch, they constantly migrate to lower voltage with the increased cycles, meaning that the formation of spinel phase. Comparing with LMNC, the variation degree of the oxidation peaks and reduction peaks for LMNA are smaller, indicating the suppressed phase transition upon the long-term cycling by the modified Li@Mn₆ superstructure units.

To further prove the reduced phase transition in LMNA, the ex situ XRD and TEM have been performed. The ex situ XRD patterns and the enlarged (003) and (104) peaks after the 1st, 2nd, 10th, 50th, and 100th cycle at 0.1 C are shown in Figure S14 in the Supporting Information. The intensity and peak position are normalized according to the strongest peak (220) of Al (65.099°). (003) peaks for LMNC cathode distinctly become broadened after the 50th and 100th cycle, and the intensity ratio of (003)/(104) becomes smaller after the 100th cycle, demonstrating the structure becomes more disordered after long cycles. On the contrary, these phenomena are not observed in LMNA cathode, indicating the stable structure during cycling. The local structure changes are further examined in cycled LMNC and LMNA cathodes. HRTEM images and the corresponding FFT maps after the 1st, 50th, and 100th cycle are shown in Figure 5. After the first cycle, the spinel phase forms at the surface for both of LMNC and LMNA cathodes (Figure 5a,d), and LMNC has a thicker spinel layer compared with LMNA cathode, further demonstrating the enhanced reversibility of oxygen redox after Al substitution. After 50 cycles, the spinel phase at the surface of LMNA cathode changes a little, still about 15-20 nm (Figure 5b). In sharp contrast, the spinel phase in LMNC cathode is thicker than 50 nm (Figure 5e). After 100th cycle, the spinel phase at the surface of LMNA cathode is transformed to rock-salt phase (Figure 5f), providing a great protection for the layered structure in the bulk. For LMNC cathode, the spinel phase continuously spreads into the bulk (Figure 5c). Combining the CV, XRD, and HRTEM results mentioned above, it could be concluded that the harmful phase transition has been restricted after the modification of Li@Mn₆ superstructure units in LMNA.

In addition, we further collected SEM images of LMNC and LMNA after 500 cycles to study the influences of long-term cycling on the particle morphology. As shown in Figure S15 in the Supporting Information, we could not observe any secondary particle of LMNC (Figure S15a, Supporting Information), and the primary particles of LMNC are covered by the thick cathode/electrolyte interphase species (Figure S15b, Supporting Information). It indicates the complete destruction of the second particles and the severe side reactions at the particle surface. In sharp contrast, the integrity of secondary particles for LMNA is well preserved (marked by the dashed circle in Figure S15c, Supporting Information), and the surface of primary particle is relatively clean (Figure S15d, Supporting Information), hinting the excellent structural stability both on the secondary particle and primary particle level.

2.6. Correlating the Local Structural Modification with the Improved Cycling Stability

The mechanism of the promoted cycling stability of LMNA with the modified Li@Mn $_6$ superstructure units can be summarized here. In **Figure 6**a, the crystal structure of LMNC can be divided into the ordered Li $_2$ MnO $_3$ domain and the cationic-disordered LiNi $_2$ / $_3$ Co $_1$ / $_3$ O $_2$ domain. In the TM layers of Li $_2$ MnO $_3$ component (marked by the blue dashed rectangle), the aggregated Li@Mn $_6$ superstructure units would bring with irreversible oxygen redox and vigorous TM migration, which induces the

16146840, 2021, 37, Downloaded from https://advanced.onlinelibrary.wiley.com/doi/10.1002/acmm.202101962 by University Town Of Shenzhen, Wiley Online Library on [24/11/2025]. See the Terms and Conditions (https://onlinelibrary.wiley.com/term

and-conditions) on Wiley Online Library for rules of use; OA articles are governed by the applicable Creative Commons

www.advancedsciencenews.com www.advenergymat.de

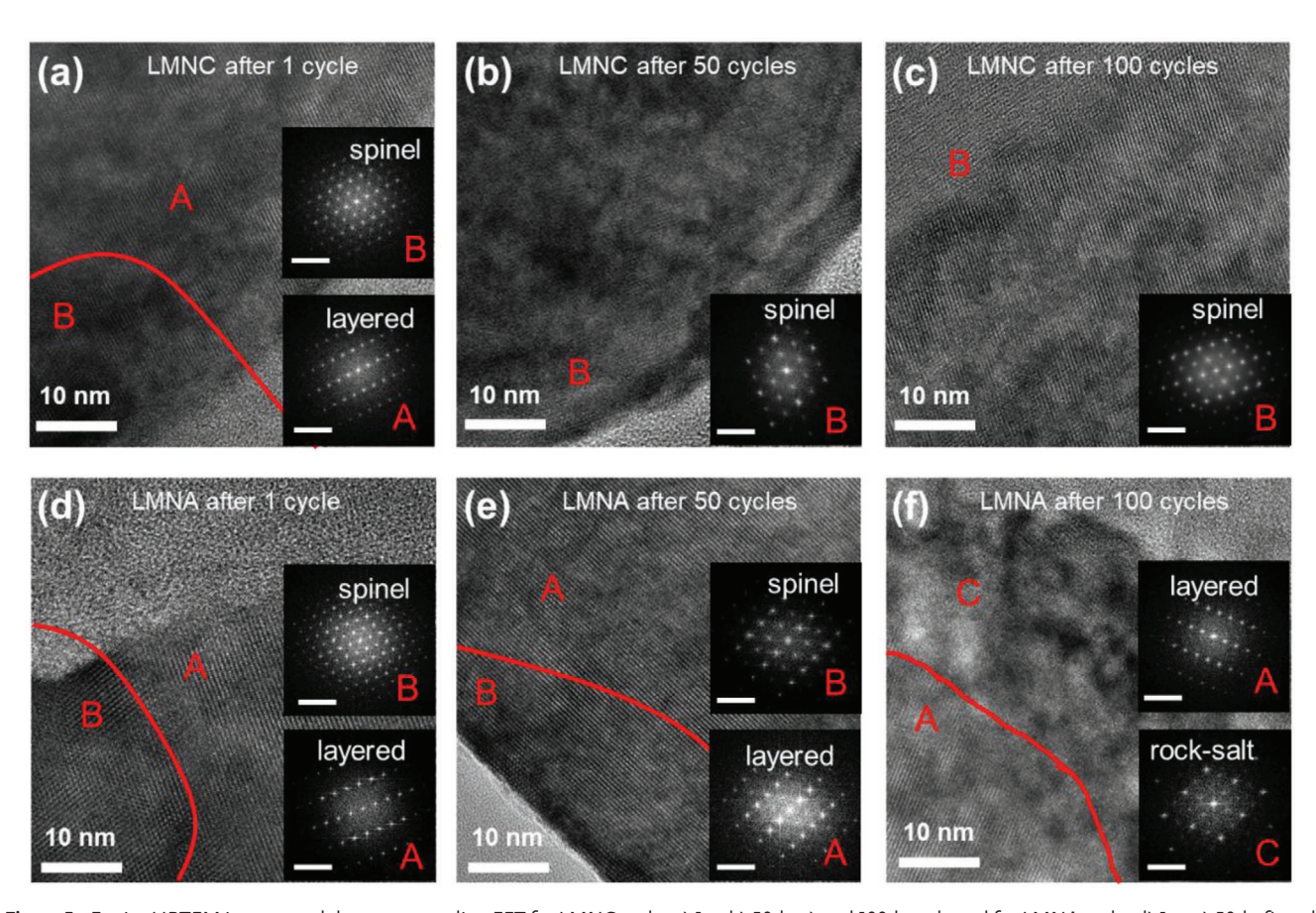


Figure 5. Ex situ HRTEM images and the corresponding FFT for LMNC at the a) 1st, b) 50th, c) and 100th cycle and for LMNA at the d) 1st, e) 50th, f) and 100th cycle. The layered region, spinel region, and rock-salt region are, respectively, marked by A, B, and C. The scale bars in the FFT maps are 5 1 nm⁻¹.

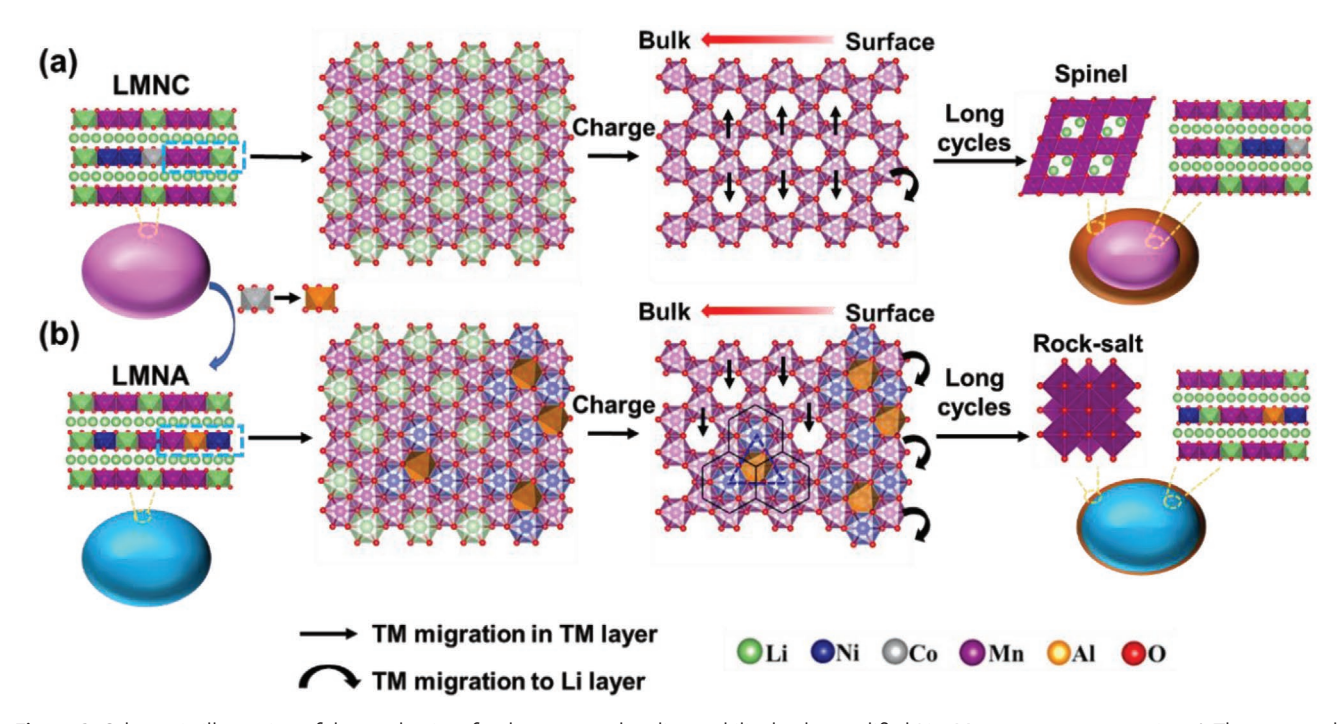


Figure 6. Schematic illustration of the mechanism for the promoted cycling stability by the modified Li@Mn₆ superstructure units. a) The structural degradation mechanism for LMNC during cycling. b) The enhanced structural stability for LMNA by Al substitution.

www.advenergymat.de

ADVANCED ENERGY MATERIALS

1614849, 2021, 37, Dwnholaded from https://atvanced.onlinelibrary.wiely.com/oi/010.002/aem.20.2010/962 by University Town Of Shezhen, Wiley Online Library on [2411.0225]. See the Terms and Conditions (https://onlinelibrary.wiely.com/terms-and-conditions) on Wiley Online Library for rules of use; OA articles are governed by the applicable Centure Commons

formation of spinel phase at the surface when charged to high potentials.^[14-16] With the long cycles, the spinel structure at the surface gradually penetrates into the bulk, which causes a wide range of spinel structure, resulting in the capacity fading and voltage decay. After Al substitution of Co (Figure 6b), the Al ions occupy the 4g sites (Mn) in Li@Mn₆ superstructure units, leading to the replacement of the central Li ions in Li@Mn₆ units by Ni²⁺. Such Ni@(Al, Mn)₆ superstructure units would act as the stable motif in the delithiated TM layers (marked by the blue triangle), greatly inhibiting TM migration and suppressing the layered/spinel phase transition in the bulk. Such motifs can also disrupt the aggregated Li-O-Li configuration partly, and make the oxygen redox become more reversible. In addition, more Ni²⁺ was located at the surface than in the bulk through the above quantitative analysis of Ni L-edge sXAS in TEY and TFY modes. It hints more Ni@(Al, Mn)₆ superstructure units at the particle surface, which may be responsible for the formation of the stable rock-salt layer at the particle surface, also benefiting to the long-term cyclability.

3. Conclusion

In summary, a new Co-free Li-rich layered oxide Li[Li_{1/4}Mn_{1/2}Ni_{1/6}Al_{1/12}]O₂ was successfully designed and prepared through Al substitution of Co. Combining the structure refinement of the SXRD pattern and the local structural analysis through atomic-resolution HAADF-STEM and XAS, the impact of Al substitution on the local structure and the electrochemical performance was systemically unveiled. The introduced Al ions occupied the 4g (Mn) sites in Li@Mn₆ superstructure units, which further induced the partial replacement of the central Li ions in Li@Mn₆ superstructure units by Ni²⁺ to balance the local charge, forming Li/Ni antisites in TM layers. Such modifications of Li@Mn₆ superstructure units make Li ions in TM layers distribute more uniformly. These structure changes suppressed the over-high oxygen redox activation, and decreased the variation along the c direction during charge/discharge, improving the structural stability. Thus, the superior long-term cycling stability was obtained in LMNA, offering a capacity retention of 91.8% after 100 cycles at 0.1 C and a capacity retention of 91.4% after 500 cycles at 1 C. This work provides an indepth understanding of the impacts of Al substitution on the local structure. More importantly, it stresses the modification of superstructure units to improve the electrochemical performance of Li-rich cathodes.

4. Experimental Section

Preparation of LMNC and LMNA: The precursors of LMNC and LMNA were synthesized by a sol–gel method. $C_2H_3O_2Li\cdot 2H_2O,$ $C_4H_6O_4Ni\cdot 4H_2O,$ $C_4H_6O_4Nn\cdot 4H_2O,$ $C_4H_6O_4Co\cdot 4H_2O,$ and AlNO_3 (Sinopharm Chemical Reagent Co., Ltd.) were mixed according to the stoichiometric ratios in LMNC and LMNA. Appropriate amounts of citric acid and polyvinylpyrrolidone (PVP-K30) (Aladdin Reagent Co., Ltd.) were used as chelating agents. Then the mixture was stirred to dry at 90 °C and subsequently annealed at 500 °C for 3 h in air atmosphere. The obtained precursors of LMNC and LMNA were rubbed in an agate mortar and annealed at 800 °C for 10 h under oxygen atmosphere to obtain LMNC and LMNA.

Materials Characterizations: The crystal structures of LMNC and LMNA were characterized by high power XRD and SXRD. The high power XRD patterns were collected by a Bruker D8-Advance diffractometer using Cu-Kα radiation at 45 kV and 100 mA. The structural evolution of LMNC and LMNA cathodes in the first cycle were tracked by in situ SXRD. The SXRD patterns were collected at Sector 11–ID–C of the Advanced Photon Source (APS) at Argonne National Laboratory. The wavelength of the X-ray beam was 0.1173 Å. Rietveld refinements of XRD and SXRD patterns were carried out by General Structure Analysis Software (GSAS) package with the EXPGUI interface.^[38,39]

The XAS experiments were performed at the Shanghai Synchrotron Radiation Facility (SSRF), under the storage ring conditions of 3.5 GeV and 220 mA current. The L-edge of Ni/Co/Mn and the K-edge of Al/O sXAS spectra were measured at beamline 02B02 of the SiP·ME² platform. Beamline 02B02 was a bending magnet beamline, which provided photons with energy range from 50 to 2000 eV. The photon flux was about 10¹¹ photons s⁻¹ and the energy resolving power $E/\Delta E$ was up to 13 000@250 eV. The beam size at the sample was set to $150 \, \mu m \times 50 \, \mu m$. The spectra were collected using surface-sensitive TEY and bulk-sensitive TFY modes simultaneously at room temperature in an ultrahigh vacuum chamber. The photon energy was calibrated with the spectra of the reference samples CoO, MnO, NiO, and SrTiO₃, which were measured simultaneously. [40] The K-edge of Ni/Co/Mn XAFS was measured at beamline 11B. This bending magnet beamline delivered monochromatic photon with energies from 5 to 30 keV. The photon flux was 5×10^{11} photons s⁻¹ and the resolving power $E/\Delta E$ was up to 5000@10 keV. These spectra were collected using total fluorescence yield method with the sample chamber filled with helium and nitrogen gas. The XAFS spectra were calibrated using Ni/Co/Mn foil spectra. The raw spectra were processed and normalized by applying Athena software packages.^[41]

The chemical composition analysis was performed by ICP-OES. The morphology and the corresponding element distribution were characterized by SEM (ZEISS Supra 55 field emission SEM) and the attached EDS. The local structure was characterized by TEM (FEI TecnaiG2 F30). STEM image of LMNA was taken on a Thermo Fisher Themis electron microscope operated at 300 kV, with a convergence angle of 25 mrad, and a collection angle of ≈6–32 mrad for differential phase contrast (DPC) imaging and 63–200 mrad for HAADF imaging.

Electrochemical Characterizations: Active materials, acetylene black carbon, and polyvinylidene fluoride were mixed with the weight ratio of 7:2:1 and poured into N-methyl pyrrolidone solvent, then stirred for 10 h to obtain a well-mixed slurry. Then the slurry was casted on the Al foil and dried at 110 °C. Coin cells (CR2032) were assembled in an argonfilled glove box with water and oxygen below 1 ppm. Pure lithium foil was used as the counter electrode and the polymer membrane was utilized as the separator. The electrolyte was 1 m lithium hexafluorophosphate (LiPF₆) solution in ethylene carbonate (EC) and ethyl methyl carbonate (EMC) in the volume ratio of 2:5. The as-assembled cells were charged and discharged in galvanostatic mode by NEWARE system. CV (at the scan rate of 0.1 mV s $^{-1}$) and electrochemical impedance spectroscopy (from 10^5 to 10^{-1} Hz, with a voltage amplitude of 10 mV) results were collected by an electrochemical workstation (1400 cell test system, Solartron).

Supporting Information

Supporting Information is available from the Wiley Online Library or from the author

Acknowledgements

Z.L. and Y.L. contributed equally to this work. The authors acknowledge support from the National Key R&D Program of China (2016YFB0700600), Natural Science Foundation of China (grants no.



ADVANCED ENERGY

16146849, 2021, 37, Dwnholaded from https://advanced.onlinelibrary.wiely.com/oi/0101002/aem.20.2101962 by University Town Of Shenzhen, Wiley Online Library on [24111025]. Se the Terms and Conditions (https://onlinelibrary.wiely.com/terms-and-conditions) on Wiley Online Library for rules of use; OA articles are governed by the applicable Creative Commons

www.advancedsciencenews.com www.advenergymat.de

11227902), the Shenzhen Science and Technology Research Grant (no. JCYJ20200109140416788), the Chemistry and Chemical Engineering Guangdong Laboratory (grant no. 1922018), the National Key R&D Program of China (2020YFB0704500), and the China Postdoctoral Science Foundation (no. 2020M680198).

Conflict of Interest

The authors declare no conflict of interest.

Data Availability Statement

The data that supports the findings of this study are available in the supplementary material of this article.

Keywords

Al substitution, Co-free Li-rich cathodes, $Li@Mn_6$ superstructure units, Li-ion batteries, local structural modification

Received: June 28, 2021 Revised: July 23, 2021 Published online: August 18, 2021

- [1] B. Dunn, H. Kamath, J. M. Tarascon, Science 2011, 334, 928.
- [2] M. M. Thackeray, C. Wolverton, E. D. Isaacs, Energy Environ. Sci. 2012 5 7854
- [3] J. M. Tarascon, M. Armand, Nature 2001, 414, 359.
- [4] B. Xu, D. N. Qian, Z. Y. Wang, Y. S. L. Meng, Mater. Sci. Eng., R 2012, 73, 51.
- [5] Z. H. Lu, L. Y. Beaulieu, R. A. Donaberger, C. L. Thomas, J. R. Dahn, J. Electrochem. Soc. 2002, 149, A778.
- [6] M. M. Thackeray, C. S. Johnson, J. T. Vaughey, N. Li, S. A. Hackney, J. Mater. Chem. 2005, 15, 2257.
- [7] J. Zheng, S. Myeong, W. Cho, P. Yan, J. Xiao, C. Wang, J. Cho, J.-G. Zhang, Adv. Energy Mater. 2017, 7, 1601284.
- [8] R. Shunmugasundaram, R. S. Arumugam, J. R. Dahn, Chem. Mater. 2015, 27, 757
- [9] M. Gu, I. Belharouak, J. Zheng, H. Wu, J. Xiao, A. Genc, K. Amine, S. Thevuthasan, D. R. Baer, J.-G. Zhang, N. D. Browning, J. Liu, C. Wang, ACS Nano 2013, 7, 760.
- [10] D. Mohanty, A. S. Sefat, S. Kalnaus, J. Li, R. A. Meisner, E. A. Payzant, D. P. Abraham, D. L. Wood, C. Daniel, J. Mater. Chem. A 2013. 1, 6249.
- [11] Y. Liu, D. Ning, L. Zheng, Q. Zhang, L. Gu, R. Gao, J. Zhang, A. Franz, G. Schumacher, X. Liu, J. Power Sources 2018, 375, 1.
- [12] S. Zhao, B. Sun, K. Yan, J. Zhang, C. Wang, G. Wang, ACS Appl. Mater. Interfaces 2018, 10, 33260.
- [13] Y. Zhang, W. Zhang, S. Shen, X. Yan, A. Wu, J. Yin, J. Zhang, J. Power Sources 2018, 380, 164.
- [14] J. Hwang, S. Myeong, W. Jin, H. Jang, G. Nam, M. Yoon, S. H. Kim, S. H. Joo, S. K. Kwak, M. G. Kim, J. Cho, Adv. Mater. 2020, 32, 2001944.

- [15] Z. Zhuo, K. Dai, R. Qiao, R. Wang, J. Wu, Y. Liu, J. Peng, L. Chen, Y.-D. Chuang, F. Pan, Z.-X. Shen, G. Liu, H. Li, T. P. Devereaux, W. Yang, Joule 2021, 5, 975.
- [16] D. H. Seo, J. Lee, A. Urban, R. Malik, S. Kang, G. Ceder, *Nat. Chem.* 2016, 8, 692.
- [17] J. Hwang, S. Myeong, E. Lee, H. Jang, M. Yoon, H. Cha, J. Sung, M. G. Kim, D.-H. Seo, J. Cho, Adv. Mater. 2021, 33, 2100352.
- [18] H. Zheng, C. Zhang, Y. Zhang, L. Lin, P. Liu, L. Wang, Q. Wei, J. Lin, B. Sa, Q. Xie, D.-L. Peng, Adv. Funct. Mater. 2021, 31, 2100783.
- [19] P. K. Nayak, J. Grinblat, M. Levi, E. Levi, S. Kim, J. W. Choi, D. Aurbach, Adv. Energy Mater. 2016, 6, 1502398.
- [20] W. Jiang, C. Zhang, Y. Feng, B. Wei, L. Chen, R. Zhang, D. G. Ivey, P. Wang, W. Wei, Energy Storage Mater. 2020, 32, 37.
- [21] B. Seteni, N. Rapulenyane, J. C. Ngila, H. Luo, *Mater. Today: Proc.* 2018, 5, 10479.
- [22] C. C. Wang, Y. C. Lin, P. H. Chou, RSC Adv. 2015, 5, 68919.
- [23] Y. L. Wang, X. Huang, F. Li, J. S. Cao, S. H. Ye, RSC Adv. 2015, 5, 49651.
- [24] W. C. Yan, Y. Xie, J. C. Jiang, D. Y. Sun, X. D. Ma, Z. G. Lan, Y. C. Jin, ACS Sustainable Chem. Eng. 2018, 6, 4625.
- [25] A. Dianat, N. Seriani, M. Bobeth, G. Cuniberti, J. Mater. Chem. A 2013, 1, 9273.
- [26] Z. Li, N. A. Chernova, J. J. Feng, S. Upreti, F. Omenya, M. S. Whittingham, J. Electrochem. Soc. 2012, 159, A116.
- [27] B. Guo, J. Zhao, X. Fan, W. Zhang, S. Li, Z. Yang, Z. Chen, W. Zhang, Electrochim. Acta 2017, 236, 171.
- [28] K. Luo, M. R. Roberts, R. Hao, N. Guerrini, D. M. Pickup, Y.-S. Liu, K. Edstrom, J. Guo, A. V. Chadwick, L. C. Duda, P. G. Bruce, *Nat. Chem.* 2016, 8, 684.
- [29] D. Alders, L. H. Tjeng, F. C. Voogt, T. Hibma, G. A. Sawatzky, C. T. Chen, J. Vogel, M. Sacchi, S. Iacobucci, *Phys. Rev. B* **1998**, *57*, 11623
- [30] A. Mandziak, G. D. Soria, J. E. Prieto, M. Foerster, J. de la Figuera, L. Aballe, *Nanoscale* 2020, 12, 21225.
- [31] R. Qiao, L. A. Wray, J.-H. Kim, N. P. W. Pieczonka, S. J. Harris, W. Yang, J. Phys. Chem. C 2015, 119, 27228.
- [32] T. Risthaus, D. Zhou, X. Cao, X. He, B. Qiu, J. Wang, L. Zhang, Z. Liu, E. Paillard, G. Schumacher, M. Winter, J. Li, J. Power Sources 2018, 395, 16.
- [33] H. Yu, Y. Qian, M. Otani, D. Tang, S. Guo, Y. Zhu, H. Zhou, Energy Environ. Sci. 2014, 7, 1068.
- [34] S. Hy, F. Felix, J. Rick, W.-N. Su, B. J. Hwang, J. Am. Chem. Soc. 2014, 136, 999.
- [35] Y. Cai, L. Ku, L. Wang, Y. Ma, H. Zheng, W. Xu, J. Han, B. Qu, Y. Chen, Q. Xie, D.-L. Peng, Sci. China Mater. 2019, 62, 1374.
- [36] X.-D. Zhang, J.-L. Shi, J.-Y. Liang, Y.-X. Yin, J.-N. Zhang, X.-Q. Yu, Y.-G. Guo, Adv. Mater. 2018, 30, 1801751.
- [37] M. A. Cambaz, B. P. Vinayan, H. Euchner, R. E. Johnsen, A. A. Guda, A. Mazilkin, Y. V. Rusalev, A. L. Trigub, A. Gross, M. Fichtner, ACS Appl. Mater. Interfaces 2018, 10, 21957.
- [38] A. C. Larson, R. B. Von Dreele, GSAS General Structure Analysis System, Los Alamos National Laboratory, Los Alamos, NM 1990.
- [39] B. H. Toby, J. Appl. Crystallogr. 2001, 34, 210.
- [40] G. Ren, N. Zhang, X. Feng, H. Zhang, P. Yu, S. Zheng, D. Zhou, Z. Tian, X. Liu, Chin. Phys. B 2020, 29, 016101.
- [41] B. Ravel, M. Newville, J. Synchrotron Radiat. 2005, 12, 537.